A simulation tool for physics-informed control of biomimetic soft robotic arms

Bartosz Kaczmarski[1], Alain Goriely[2], Ellen Kuhl[1], Derek E. Moulton[2]

***Abstract*—Due to an infinite number of degrees of freedom, soft robotic arms remain challenging to control. Past work has drawn inspiration from biological structures–for example the elephant trunk–to design and control biomimetic soft robotic arms. However, to date, the models used to inform the control of biomimetic arms lack generalizability, and largely rely on qualitative assumptions. Here, we present a computationally efficient methodology to control fiber-based slender soft robotic arms inspired by the theory of active filaments. Our approach seeks to optimize fibrillar activation under prescribed control objectives. We evaluate the methodology under various control objectives, and consider several distinct fiber architectures. Our results suggest that we can efficiently compute fibrillar activations towards the imposed control objective. Based on our findings, we discuss the effect of actuator complexity on actuation capabilities as a function of the number and arrangement of fibers. Our method can be applied universally towards the objective-based control and design of slender soft robotic arms with embedded fibers.**

***Index Terms*—Soft robotics, physics-informed robotic control, fiber-reinforced robotic arms, continuum modeling.**

I. INTRODUCTION

In the field of robotics, we distinguish four primary classes of robotic arms: rigid, discrete hyper-redundant, hard continuum, and soft arms [1]. While optimal control methods for rigid serial manipulators have been well-established in the past several decades [2]–[5], the control of soft robotic arms remains a significant challenge, and constitutes an area of active investigation [6], [7]. The challenges in the control and mathematical modeling of soft structures lie in the mechanical intricacies governing their continuous deformation. Specifically, in contrast to rigid robots with a finite number of degrees of freedom, soft-robotic arms are described by an infinite number of degrees of freedom [8], as every material point in the elastic continuum of the soft robot can, in principle, undergo arbitrary deformations.

Designing control methods for systems with an infinite number of degrees of freedom is a non-trivial task [9], so computational mechanics models are invaluable for describing the deformations of soft-robotic arms as a function of the actuation input. That is, having access to an explicit relationship between the actuation input and the resulting deformation of a given soft-robotic arm enables the development of a robust mechanical control framework for that robotic design. A considerable body of work has been committed to formulating such models [10].

[1]Bartosz Kaczmarski and Ellen Kuhl are with the Living Matter Laboratory, Stanford University, Stanford, California, USA (e-mail: bartoszk@stanford.edu, ekuhl@stanford.edu).

[2]Derek Moulton and Alain Goriely are with the Mathematical Institute, University of Oxford, United Kingdom (e-mail: moulton@maths.ox.ac.uk, alain.goriely@maths.ox.ac.uk).

In particular, researchers have devoted special attention to designing and modeling soft-robotic redarms inspired by biological structures in the animal kingdom, such as the elephant trunk or the octopus arm [11]–[14]. However, the models and control methods developed for these biomimetic designs lack generalizability, as their assumptions are specialized for their respective engineering design implementations. Further, they often rely on a geometrical discretization of the domain to represent the infinite-degree-of-freedom system using a simplified model with a finite number of degrees of freedom, which can sacrifice model fidelity. Finally, theoretical models of biomimetic actuators are frequently developed under qualitative assumptions that are difficult to validate for generic soft robot designs. For instance, they assume purely kinematic descriptions of the underlying actuation or employ linear elasticity formulations that do not generalize to finite deformations.

To improve upon the past modeling approaches for biomimetic robots, we propose a computational tool for the quasi-static control of biomimetic soft robotic arms based on the active filament model [15] and the morphoelastic rod theory [16]. Most slender biological arms—that could be readily used as a biomimetic inspiration for soft actuator architecture design—consist of some arrangement of muscle fibers. As such, our model considers a family of soft-robotic arms that are actuated via the activation of a fiber field embedded in the slender soft arm. Our approach is similar to some of the past modeling developments for soft manipulators [17]–[19], in that it utilizes dimensional reduction to characterize the slender structure of the robotic arm as a one-dimensional Kirchhoff rod [20]. However, the active filament model employed in this work is derived from a rigorous three-dimensional continuum-mechanics formulation of the fiber-reinforced arm, for a generalized geometry of the embedded fiber field. Thus, any notable loss in fidelity of the control framework presented here is only due to the dimensional reduction; otherwise, the model is mechanically accurate with respect to the physical phenomena governing the deformations of the filamentary arm.

II. FIBER-BASED SOFT ARM MECHANICS

Before describing the control approach itself, we briefly summarize the morphoelastic filament theory [16] and the active filament model [15].

A. Morphoelastic filament theory

We use the theory of morphoelasticity to describe the mechanics of a fiber-based robotic arm [16]. This continuum-based theory considers a general three-dimensional tubular body $\mathcal{B}_0 \subset \mathbb{R}^3$ representing the filament. We describe the

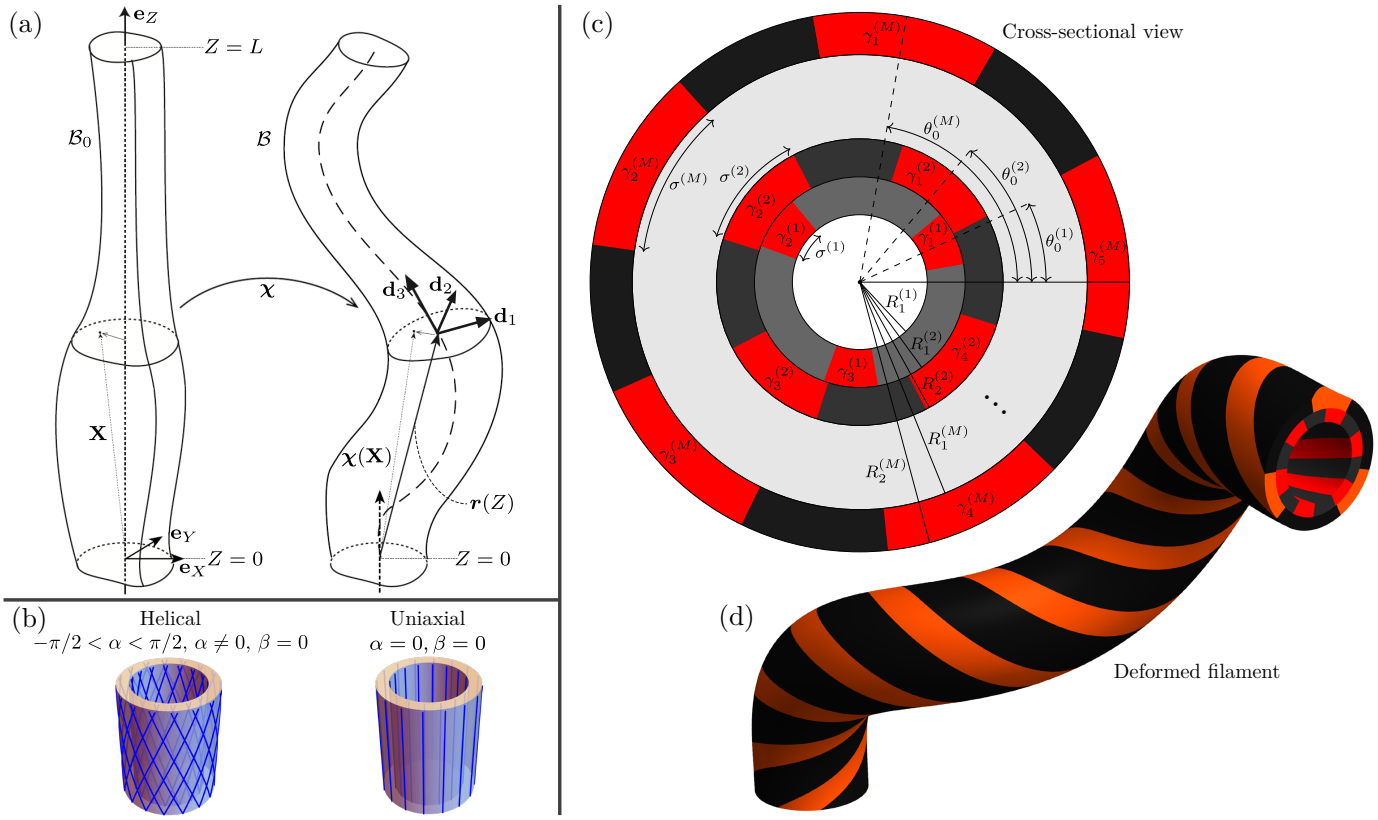


Fig. 1. Schematic description of the active filament model. (a) The morphoelastic filament theory in [16] considers the continuum mechanics of a filament with a deformation map $\boldsymbol{\chi} : \mathcal{B}_0 \to \mathcal{B}$. The form of $\boldsymbol{\chi}$ is restricted to represent the dimensionally reduced geometry of the filament consisting of the centerline $\boldsymbol{r}(Z)$ and the director basis functions $\{\mathbf{d}_1(Z), \mathbf{d}_2(Z), \mathbf{d}_3(Z)\}$. (b) The active filament model in [15] assumes an activation tensor field $\mathbf{G}$ acting along a fiber field embedded in the filament. Our analysis focuses on helical fiber fields activated in tubular regions of $\mathcal{B}_0$. The uniaxial field is a special case of the helical fiber field with $\alpha = 0$. (c) Piecewise uniform activation functions $\gamma^{(1)}(\theta), \ldots, \gamma^{(M)}(\theta)$ are assumed for robotic arm control. $R_1^{(i)}$, $R_2^{(i)}$ are the inner and outer radii of the i-th ring, respectively. The activation in the j-th annular sector of the i-th ring is denoted $\gamma_j^{(i)}$. In the i-th ring, $\theta_0^{(i)}$ is the angular offset of all $N^{(i)}$ activated sectors, and $\sigma^{(i)}$ defines the angular width of each sector. (d) The active annular sectors in each ring (shown in red) wind around the tubular body of the filament, as dictated by the prescribed helical fiber field. The visualized filament consists of $M = 2$ rings of helical fibers. Subfigure (a) is adapted from [16], and subfigures (b)-(d) are adapted from [15].

active material change at each point in the continuum $\mathcal{B}_0$ through a local tensor field $\mathbf{G}$, which creates a deformation $\boldsymbol{\chi}$, producing the current configuration $\mathcal{B} \subset \mathbb{R}^3$ (Fig. 1a).

Importantly, the specific form of $\boldsymbol{\chi}$ is limited to deformations pertinent to a dimensionally reduced representation of the filament. This facilitates the interpretability of the simulation results and significantly improves the computational efficiency of the implementation. Specifically, we reduce the three-dimensional continuum $\mathcal{B}$ to a space curve $\boldsymbol{r} : [0, L] \to \mathbb{R}^3$, the centerline, where L is the length of the filament in the reference configuration $\mathcal{B}_0$. The argument of the centerline function is the material coordinate Z. The director basis $\{\mathbf{d}_1, \mathbf{d}_2, \mathbf{d}_3\} : [0, L] \to \mathbb{R}^3$ is attached to $\boldsymbol{r}(Z)$ for all Z, and represents the material orientation of the cross section as a function of Z. Fig. 1a visualizes this dimensional reduction, which is similar to the well-established Kirchhoff theory for the mechanics of thin rods [20]. However, the advantage of the morphoelastic theory lies in the fact that it considers the complete continuum mechanics of finite deformation, starting from a rigorous construction of the deformation gradient $\mathbf{F} = \text{Grad}\ \boldsymbol{\chi}$.

The mathematical procedure describing the deformation $\boldsymbol{\chi}$ relies on the commonly applied multiplicative decomposition of the deformation gradient $\mathbf{F}$ into the elastic part $\mathbf{A}$ and the growth part $\mathbf{G}$, i.e., $\mathbf{F} = \mathbf{AG}$. For a given growth tensor $\mathbf{G}$, the form of $\mathbf{F}$ is then derived under the assumption of a limited family of permissible deformations $\boldsymbol{\chi}$ dictated by the previously described dimensional reduction. To obtain the deformed configuration of the filament, we minimize the total energy of the system over all deformations permitted by the form of $\boldsymbol{\chi}$. The minimization leads to explicit expressions for the intrinsic curvatures $\hat{u}_1$, $\hat{u}_2$, $\hat{u}_3$, and extension $\hat{\zeta}$ of the filament. Importantly, these quantities are intrinsic, i.e., they characterise the unloaded filament configuration resulting from a prescribed growth field. To obtain the intrinsic shape $\boldsymbol{r}$ of the robotic arm, we integrate the curvatures and extension using the differential relations

$$\boldsymbol{r}'(Z) = \hat{\zeta}(Z)\mathbf{d}_3(Z), \quad \mathbf{d}_i'(Z) = \hat{\zeta}(Z)\hat{\mathbf{u}}(Z) \times \mathbf{d}_i(Z), \qquad (1)$$

for $i = 1, 2, 3$, where $\hat{\mathbf{u}} = (\hat{u}_1, \hat{u}_2, \hat{u}_3)$ [16].

For given intrinsic properties of the filament and given external loading, we can integrate the filament's equilibrium shape by using the filament force and moment balance equations

[21]. This allows us to incorporate any loading scenario into the mechanics of the simulated system.

This generalized treatment provides a framework for computing the deformation of filaments subject to arbitrary growth tensor fields $\mathbf{G}$. The active filament model adopts this framework under a particular choice of $\mathbf{G}$ that describes a distributed activation of fibers embedded in the filament.

B. Active filament model

The active filament model [15] is a specialized application of the general theory of morphoelastic filaments. Namely, active filaments assume that the tensor field $\mathbf{G}$ satisfies the incompressibility constraint, $\det(\mathbf{G}) = 1$. From now on, we refer to the tensor field $\mathbf{G}$ as *activation* rather than growth, since the constraint of volume preservation implies no deposition of new material in $\mathcal{B}_0$. Instead, an activation $\mathbf{G}$ effectively quantifies the local effort of the material to induce deformation throughout $\mathcal{B}_0$. Incompressibility is particularly applicable to soft-robotic actuation mediated by the activation of contractile or extensible fibers. The prevalence of such a robotic design warrants further specification of the form of the activation $\mathbf{G}$ in the model. Specifically, we consider an active fiber architecture following a fiber direction field $\mathbf{m}$ that is embedded in the filament body [15], and express the fiber field in a cylindrical basis,

$$\mathbf{m} = \sin\alpha \sin\beta\ \mathbf{e}_R + \sin\alpha\cos\beta\ \mathbf{e}_\Theta + \cos\alpha\ \mathbf{e}_Z, \quad (2)$$

where α and β are arbitrary functions of the radius R, the polar angle Θ, and the material coordinate Z.

Fiber geometries in soft robots are usually not arranged arbitrarily, but often follow helical architectures [22]. The theory of active filaments [15] narrows the underlying kinematics down to a specialized case of the activation field. In particular, we prescribe $\mathbf{G}$

- in a set of concentric, tubular regions $\mathcal{R}^{(i)} = \{R \in [R_1^{(i)}, R_2^{(i)}], \Theta \in [0, 2\pi), Z \in [0, L]\} \subset \mathcal{B}_0$ called rings,
- along a helical fiber field $\mathbf{m}^{(i)}$ in each $\mathcal{R}^{(i)}$, such that $\alpha^{(i)} \in [0, \pi/2]$ and $\beta^{(i)} = 0$,

for $i = 1, \ldots, M$. Importantly, a helical angle $\alpha^{(i)} = 0$ is a special case of a helical field $\mathbf{m}$ corresponding to a uniaxial fiber field. Fig. 1b illustrates the activation geometry for $M = 1$. In this setting, the deformation of the filament is generated by the contraction or extension of the helically-arranged fibers embedded in $\mathcal{R}^{(1)}, \ldots, \mathcal{R}^{(M)}$. To characterize the fiber activation throughout the entire filament body, we define an *activation function* $\gamma^{(i)}(\theta)$ in each cross section $\mathcal{R}^{(i)}$. Following [15], we then obtain the analytical expressions for $\hat{\mathbf{u}}$ and $\hat{\zeta}$ as functions of $\gamma^{(i)}(\theta)$, $\alpha^{(i)}$ and the geometries of $\mathcal{R}^{(i)}$ to integrate the shape of the filament for an arbitrary activation:

$$\hat{\zeta} = 1 + \frac{1}{2R_0^2} \sum_{i=1}^{M} a_0^{(i)} \delta_0^{(i)}, \quad (3)$$

$$\hat{u}_1 = -\frac{4}{3R_0^4} \sum_{i=1}^{M} A^{(i)} \delta_1^{(i)} \sin\left(\varphi^{(i)} - \frac{Z}{R_2^{(i)}} \tan\alpha_2^{(i)}\right), \quad (4)$$

$$\hat{u}_2 = -\frac{4}{3R_0^4} \sum_{i=1}^{M} A^{(i)} \delta_2^{(i)} \cos\left(\varphi^{(i)} - \frac{Z}{R_2^{(i)}} \tan\alpha_2^{(i)}\right), \quad (5)$$

$$\hat{u}_3 = \frac{2}{R_0^4} \sum_{i=1}^{M} \delta_3^{(i)} a_0^{(i)}, \quad (6)$$

where $a_0^{(i)}$, $a_1^{(i)}$, $b_1^{(i)}$ are the first three Fourier coefficients of the activation distribution $\gamma^{(i)}(\theta)$, R_0 is the outer radius of the filament, $\delta_j^{(i)} = \delta_j^{(i)}(R_1^{(i)}, R_2^{(i)}, \alpha_2^{(i)}, \nu^{(i)})$ for $j \in \{1, 2, 3\}$, $\alpha_2^{(i)} = \alpha^{(i)}(R = R_2^{(i)})$ is the helical angle of the fiber field on the outer surface of the i-th ring, $\nu^{(i)}$ is the Poisson's ratio of the i-th ring, and $A^{(i)}$ and $\varphi^{(i)}$ are such that $a_1^{(i)} = A^{(i)}\cos(\varphi^{(i)})$, $b_1^{(i)} = -A^{(i)}\sin(\varphi^{(i)})$ [15]. As a final step, using (3)-(6) and (1), we compute the deformed filament shape given the activation $\gamma^{(i)}(\theta)$ of each ring.

While the proposed approach permits any form of $\gamma^{(i)}(\theta)$, we consider the case of a piecewise uniform activation $\gamma^{(i)}(\theta; \bar{\gamma}^{(i)}, \sigma^{(i)}, \theta_0^{(i)})$, in which $N^{(i)}$ annular sectors are activated, and the activation is zero in the rest of the i-th ring. The parameter set $\bar{\gamma}^{(i)} = (\gamma_1^{(i)}, \ldots, \gamma_{N^{(i)}}^{(i)})$ represents the activation values in the activated sectors of the i-th ring, while both $\sigma^{(i)}$ and $\theta_0^{(i)}$ define the geometry of the annular sectors, as depicted in Fig. 1c. The activation function $\gamma^{(i)}(\theta)$ directly mimics the actuation of a fiber-based soft continuous robot, in which macro-scale fibers are embedded in a helical pattern within an elastic continuum. Fig. 1d illustrates the three-dimensional structure of a deformed active filament. The physical fiber actuators of the soft arm are represented in the visualization by the helically winding regions of piecewise activation.

III. CONTROL METHODOLOGY

A. General quasi-static control approach

In this work, we construct the physics-based control approach under the quasi-static assumption. That is, we assume that the typical time scale of fiber activation in an actuator is long enough, that dynamic effects can be neglected. As a result, the motion of the continuum arm can be approximated as a sequence of static configurations. To ensure transient stability of these intermediate configurations in an engineered robotic solution, a PD setpoint controller paradigm established in [23] could be adapted for the active filament physics to dampen the short-scale vibrations of the soft manipulator.

Our quasi-static control methodology for fiber-based soft arms is physics-based and purely mechanistic, since we directly apply the active filament model to relate the motion of the arm to the fiber activation. In particular, in our control approach, we solve the inverse problem of computing the actuation input that causes the robotic arm to match a prescribed geometric objective $\mathcal{G}$. Most generally, we define a geometric objective as a function of the manipulator's centerline and its derivatives. In the context of the active filament theory, the activation functions $\gamma^{(i)}(\theta)$ are the actuation inputs to a soft arm that generate a certain deformation. Given some activation, we compare the resulting deformation against $\mathcal{G}$ to assess how well the deformed shape of the arm fulfils the assigned objective. To quantify this comparison, we require a metric designed to measure how closely a given deformation matches the objective $\mathcal{G}$.

The closeness of a match between the arm's deformed configuration and $\mathcal{G}$ is quantified by a cost function metric $J^{\mathcal{G}}$,

chosen for a particular $\mathcal{G}$. The goal is then to minimize $J^{\mathcal{G}}$ with respect to $\Gamma = (\gamma^{(1)}(\theta), \ldots, \gamma^{(M)}(\theta))$, so that feeding Γ into the active filament model yields a configuration matching $\mathcal{G}$. In general, for a given objective, there exist infinitely many $\gamma^{(i)}(\theta)$ (for each i) that achieve that objective, making the optimization of $J^{\mathcal{G}}$ non-convex. This ill-defined nature of the inverse problem is caused by the hyper-redundant property of soft-robotic arms with an infinite number of degrees of freedom. Therefore, we have to take special care in the minimization procedure in order to ensure that it converges to the desired optimum; e.g., by imposing optimization constraints or applying multi-start methods. Further, since computing the manipulator's centerline requires numerical integration, the gradient of $J^{\mathcal{G}}$ cannot be explicitly derived. Thus, given the non-convexity of the cost function and since an explicit form of $\nabla J^{\mathcal{G}}$ is unavailable, we utilize the Nelder-Mead simplex method to perform the global optimization with multiple randomized activation initializations. Exploring the initialization space reduces the chance of the optimization method becoming stuck in an undesirable local minimum, and strengthens the credibility of any general conclusions drawn from the optimization results. Despite the highly complex cost function landscape, soft arm control via the described optimization framework is not computationally expensive—it can be performed in real-time thanks to the analytical forms of $\hat{\mathbf{u}}$ and $\hat{\zeta}$.

Given the generalized description of the optimization problem, we particularize our approach by restricting the allowable forms of $\gamma^{(i)}(\theta)$ to the piecewise uniform activation function $\gamma^{(i)}(\theta; \bar{\gamma}^{(i)}, \sigma^{(i)}, \theta_0^{(i)})$ described earlier. Under this piecewise activation assumption, we seek to minimize $J^{\mathcal{G}}$ with respect to the set of all sector-wise activation values $\boldsymbol{\Gamma} = (\bar{\gamma}^{(1)}, \ldots, \bar{\gamma}^{(M)})$ to obtain the minimizing activation parameter set $\boldsymbol{\Gamma}^{\mathcal{G}}$. Consequently, the continuous quasi-static path of the arm towards the objective $\mathcal{G}$ can be generated naturally as a sequence of scaled parameter sets $\bar{\gamma}^{(i)} = \gamma_0 \bar{\gamma}_{\mathcal{G}}^{(i)}$, where $\gamma_0 \in [0, 1]$.

Finally, as an optional element of the control methodology, the optimization procedure can be subject to an arbitrary set of constraints $\mathcal{C}(\boldsymbol{\Gamma}; \boldsymbol{r}, \boldsymbol{r}', \ldots)$. The motivation for constrained optimization is twofold. Firstly, the constraints can be used to limit the parameter space according to physical requirements. For instance, we can prevent the simulated manipulator from entering a restricted region $\mathcal{D}$ (i.e., enforce obstacle avoidance through $\mathcal{C} = \{\boldsymbol{r}(Z) \notin \mathcal{D}\}$) or ensure that the activation values and arm geometry stay within a range feasible from an engineering standpoint—e.g., $\mathcal{C} = \{\gamma_j^{(i)} \in [\gamma_{\min}, \gamma_{\max}]\}$ for activation parameters, or $\mathcal{C} = \{\|\hat{\mathbf{u}}(Z)\| \leq U_{\max}\}$ for the arm curvature. Secondly, imposing constraints can guide the global optimization process to yield more desirable optima, e.g., when multiple robotic arm configurations can match the same $\mathcal{G}$ perfectly (with $J^{\mathcal{G}} = 0$).

B. Classification of optimization objectives

The design of a particular cost function form is informed by the chosen $\mathcal{G}$. Optimization objectives relevant for spatial control of robotic arms are most readily derived from distance cost metrics. Thus, in our analysis, we distinguish three main objective classes based on such metrics, motivated by real-world actuation use cases.

Target endpoint position. This objective is used for the manipulator's endpoint to reach a specified target endpoint position $\boldsymbol{r}_{\text{end}}^{\mathcal{G}}$. The cost function is the squared Euclidean distance from the prediction to the target, i.e.,

$$J^{\mathcal{G}}(\boldsymbol{\Gamma}) = \left\| \boldsymbol{r}_{\text{end}}^{\mathcal{G}} - \boldsymbol{r}(L; \boldsymbol{\Gamma}) \right\|^2. \tag{7}$$

We distinguish this type of an optimization objective based on a class of robotic tasks in which an arm has to reach a specified location with its end effector.

Target configuration. The goal of optimizing under this objective is to match a desired integral shape $\boldsymbol{r}^{\mathcal{G}}(Z)$ of the whole arm. To allow additional control over the optimized result, the cost function is defined as a weighted sum of squared Euclidean distances from discrete points $Z_i \in \mathcal{Z}$ along the centerline prediction to points $S_i \in \mathcal{S}$ along the target centerline. That is,

$$J^{\mathcal{G}}(\boldsymbol{\Gamma}) = \sum_{S_i \in \mathcal{S},\, Z_i \in \mathcal{Z}} w_i \left\| \boldsymbol{r}^{\mathcal{G}}(S_i) - \boldsymbol{r}(Z_i; \boldsymbol{\Gamma}) \right\|^2, \tag{8}$$

where w_i are the weights associated with each pair of points. A potential use case of this objective is a task in which a continuum robotic arm has to achieve a particular target shape. For example, such a task could require the soft arm to form a tight spiral around an object to be grappled, or to assume specific configurations allowing it to navigate through obstacles.

Complex objectives. The simple objectives listed here can be modified and combined into a complex objective. For instance, combining multiple cost function forms via weighted superposition would yield complex objectives describing more intricate control goals. The cost function could also incorporate higher-order derivatives of $\boldsymbol{r}$ to, e.g., penalize deviations from a target orientation of the manipulator's end effector. Alternatively, a target end effector orientation could be imposed directly in the constraint set $\mathcal{C}$.

Almost all optimization objectives relevant from an engineering perspective can be assigned to one of the three classes described here. Throughout our work, we utilize this classification to gain insight into the behavior and performance of our optimization framework.

IV. RESULTS AND DISCUSSION

We evaluate the control approach computationally for the objective classes listed above. We further demonstrate and discuss the effect of the chosen fiber field architecture on the behavior of the fiber-based soft-robotic arm under optimization. Throughout the computations reported below, it is assumed that $\boldsymbol{r}(0) = (0, 0, 0)$, $\mathbf{d}_1(0) = (1, 0, 0)$, $\mathbf{d}_2(0) = (0, 1, 0)$, and $\mathbf{d}_3(0) = \mathbf{d}_1(0) \times \mathbf{d}_2(0)$, such that the arm is clamped at the origin with a fixed director basis.

A. Single-ring fiber fields

The activation inputs to arms with three different single-ring fiber fields ($M = 1$, $\boldsymbol{\Gamma} = \bar{\gamma}$) are optimized to match the target endpoint position $\boldsymbol{r}_{\text{end}}^{\mathcal{G}} = \frac{1}{3}(L, L, L)$, such that the orientation of the end effector is free and unconstrained. We

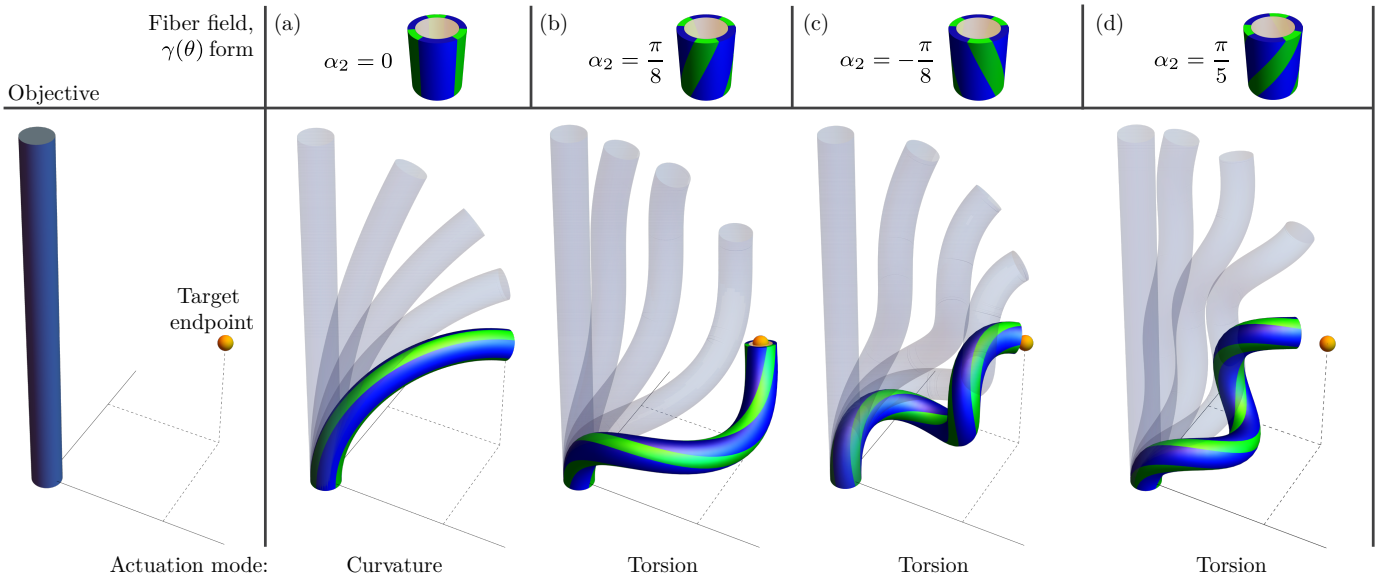


Fig. 2. Results of optimizing the fiber-based actuation input for single-ring helical fiber fields given a target endpoint objective $\boldsymbol{r}^{\mathcal{G}}_{\text{end}} = \frac{1}{3}(L, L, L)$. Three fiber field architectures were evaluated: (a) uniaxial ($\alpha_2 = 0$), (b) right-handed helical ($\alpha_2 = \pi/8$), (c) left-handed helical ($\alpha_2 = -\pi/8$), (d) right-handed helical ($\alpha_2 = \pi/5$). The uniaxial and helical fiber arrangements exhibit different geometrical methods of achieving the objective—the filament in the uniaxial case reaches the target endpoint through curvature, while the filaments with helical fibers deform primarily via torsion. The arms with fiber fields in (a) and (b) achieve the target endpoint location perfectly, but the filaments in (c) and (d) achieve the control objective with a distance deviations of $0.027L$ and $0.085L$, respectively. In each case, we enforce the optimization constraints $\mathcal{C} = \{-8 \leq \gamma_i \leq 0, \forall Z \in \mathcal{Z} : \|\hat{\mathbf{u}}(Z)\| \leq 2.2\}$, where $\mathcal{Z}$ is a discrete set of uniformly spaced coordinates $Z \in [0, L]$ with spacing $\Delta Z = L/10$. The $\gamma(\theta)$ forms were prescribed such that $N = 3$, $\theta_0 = 0$ and $\sigma = \pi/4$ in all cases. The intermediate motion paths for each of the four cases were computed using scaled activation inputs $\bar{\gamma} = \gamma_0 \bar{\gamma}^{\mathcal{G}}$, for $\gamma_0 \in \{0, 0.25, 0.5, 0.75\}$. For all cases, $L = 10$, $R_1 = 0.3$, $R_2 = 0.4$, $E = 1$, and $\nu = 1/2$.

evaluated the following fiber fields: (a) uniaxial ($\alpha_2 = 0$), (b) right-handed helical with $\alpha_2 = \pi/8$, (c) left-handed helical with $\alpha_2 = -\pi/8$, (d) right-handed helical with $\alpha_2 = \pi/5$. We enforce optimization constraints on the activation parameters with $\gamma \in [-8, 0]$, and restrict the maximum curvature by setting $U_{\text{max}} = 2.2$. The resulting optimal arm configurations are visualized in Fig. 2, together with their respective quasi-static motion paths computed via $\bar{\gamma} = \gamma_0 \bar{\gamma}^{\mathcal{G}}$. Refer to the included video for continuously animated motion paths of all evaluated simulation experiments. The minimized cost function values $J^{\mathcal{G}}$ were 0 in scenarios (a) and (b), while the endpoint distance deviation $\|\boldsymbol{r}(L) - \boldsymbol{r}^{\mathcal{G}}_{\text{end}}\|$ in (c) was $0.027L$, and $0.085L$ in (d). The corresponding minimizing parameter sets $\bar{\gamma}^{\mathcal{G}}$ are reported in Table I.

The results demonstrate that there exists a solution $\bar{\gamma}^{\mathcal{G}}$ that perfectly achieves the target endpoint position for fiber fields (a) and (b). We emphasize that the chosen $\boldsymbol{r}^{\mathcal{G}}_{\text{end}}$ is attainable in these cases partly because of the assumed filament extensibility, which permits shortening of the centerline for sufficiently negative $\bar{\gamma}$. Specifically, the series of shortening intermediate configurations along the actuation path shown in Fig. 2a illustrates that centerline contraction constitutes an important factor in achieving the prescribed $\mathcal{G}$. The ratios $L_{\boldsymbol{\Gamma}}/L$ of the length of the activated centerline to the initial length of the centereline are reported in Table I for all evaluated simulation scenarios. We recognize that some soft robotic arm designs might not allow such contraction magnitudes. Setting $\hat{\zeta} = 1$ could accommodate this design constraint, as it limits the optimization to only inextensible filaments. If some limited extensibility is permitted, we could enforce the maximum extension magnitude by adding a constraint $\hat{\zeta}(Z) < \zeta_{\text{max}}$.

Moreover, while the arm with uniaxial fibers reached $\mathcal{G}$ by increasing curvature, the arms with helical fibers attempted to match $\mathcal{G}$ primarily through torsion. Formally, uniaxial fiber architectures cannot produce torsion, since the uniform longitudinal fiber contraction results in a geometric mismatch that causes bending of the arm only along axes contained in the XY-plane. As a result, assuming uniform activation with respect to Z, curvature is the only mode of actuation that a uniaxial fiber field can utilize to match the prescribed $\mathcal{G}$. On the other hand, in agreement with the obtained results, fiber contraction along a helix woven around the manipulator should intuitively result in filament torsion. The helical fiber architectures can generate torsion since the local contraction directions of all fibers are oblique and they twist around the robotic arm with respect to the arc length.

The obtained minimizing solutions $\bar{\gamma}^{\mathcal{G}}$ were influenced by the enforced constraints. In particular, the purpose of restricting the range of activation parameters to $-8 \leq \gamma_i \leq 0$ was to avoid physically unrealistic activation magnitudes and to permit only fiber contraction rather than extension. This choice is motivated by biomimicry, as muscle fibers in animals, for instance, rely purely on contraction to produce strains necessary for biological actuation [10].

The enforced constraints have a particularly noteworthy impact on matching the prescribed control goal in the case of the left-handed fiber field. Specifically, for the arm with the fiber fields in (c) and (d), the optimization process failed to find a parameter set $\bar{\gamma}$ that would enable a perfect matching of the target endpoint objective. The reason for such a result

in (c) is that, under the imposed set of constraints $\mathcal{C}$ on the activation parameters, the left-handedness of the helical fiber field generates a left-handed helical shape of the manipulator's deformed configuration. Consequently, the handedness of the manipulator's centerline that is feasible under $\mathcal{C}$, combined with the origin boundary conditions (for $\boldsymbol{r}$ and $\{\mathbf{d}_1, \mathbf{d}_2, \mathbf{d}_3\}$), requires a configuration with a higher torsion to achieve the desired control objective. When attempting to reach the same target endpoint position, the total length of the centerline also needs to become larger in a configuration with a higher torsion. However, the constraint $\gamma_{\text{max}} = 0$ implies that $\hat{\zeta} \leq 1$, i.e., the centerline can only contract in all three of the evaluated fiber fields. Thus, the fibrillar contraction in arm (c) cannot produce a deformed configuration that achieves both sufficiently high torsion, and small enough centerline contraction for the target endpoint position to be reached exactly. If the negative activation constraint was relaxed to permit extensile fibers, then arm (c) would indeed achieve the prescribed control goal perfectly.

While the helical fiber field in (d) is right-handed, it still cannot reach the target endpoint with the given constraints. For this fiber architecture, such a limitation is due to the larger fiber angle $\alpha_2 = \pi/5$ which generally generates a significantly larger amount of twist compared to $|\alpha_2| = \pi/8$. As a result, the centerline curls into a high-torsion shape before it is able to reach the target location.

The prescribed fixed-end boundary conditions also have a considerable effect on the optimization results. In particular, the fixed-end director basis $\{\mathbf{d}_1(0), \mathbf{d}_2(0), \mathbf{d}_3(0)\}$ could be rotated around $\mathbf{e}_Z$ to reflect axial rotation of the entire robotic arm. Choosing an appropriate rotation of the fixed-end director basis in the arm in Fig. 2c can result in perfect matching of the optimization objective with $J^{\mathcal{G}} = 0$. Indeed, permitting an arbitrary boundary condition basis $\{\mathbf{d}_1(0), \mathbf{d}_2(0), \mathbf{d}_3(0)\}$ vastly expands the subspace of $\mathbb{R}^3$ reachable by the endpoint of the manipulator. As such, we enforce a fixed director basis $\{\mathbf{d}_1(0), \mathbf{d}_2(0), \mathbf{d}_3(0)\}$, because we seek to investigate the differences in actuation techniques developed by various fiber architectures, and these differences become occluded entirely whenever arbitrary $\{\mathbf{d}_1(0), \mathbf{d}_2(0), \mathbf{d}_3(0)\}$ are permitted.

B. Multi-ring fiber fields

Introducing additional rings with distinct fiber fields to the filament increases its actuation versatility. To evaluate this claim, we consider the control of filaments with three two-ring fiber fields: (a) uniaxial and right-handed helical, (b) uniaxial and left-handed helical, (c) left-handed helical and right-handed helical, (d) uniaxial and right-handed helical with a large helical angle. The optimization objectives for these two-ring fiber fields are more complex, and require more involved configurations. In particular, the four fiber fields are evaluated for two optimization objectives: (i) a target endpoint position $\boldsymbol{r}^{\mathcal{G}}_{\text{end}} = \frac{1}{3}(L, L, L)$ with the constraint $\mathcal{C} = \{\boldsymbol{r}(Z) \notin \mathcal{D}\}$, where $\mathcal{D}$ represents a cylindrical obstacle, (ii) a target configuration given by a target curve $\boldsymbol{r}^{\mathcal{G}}(t)$. In both cases, we imposed the additional constraint $\gamma \in [-8, 0]$ for the activation parameters. The deformed configurations of the filaments (a)-(d) optimized under the objectives (i) and (ii) are shown in Fig. 3. The translucent visualizations of the quasi-static motion paths are again computed through the linear scaling $\boldsymbol{\Gamma} = \gamma_0 \boldsymbol{\Gamma}^{\mathcal{G}}$ of the optimized activation. Table I contains the minimizing parameter sets $\boldsymbol{\Gamma}^{\mathcal{G}}$ corresponding to the eight cases considered in Fig. 3.

In objective (i), filaments (a)-(c) achieved the target endpoint position perfectly with $J^{\mathcal{G}} = 0$ without intersecting the introduced cylindrical obstacle. Nonetheless, the scaled activation $\boldsymbol{\Gamma} = \gamma_0 \boldsymbol{\Gamma}^{\mathcal{G}}$ for fiber field (c) results in the intersection of the obstacle at intermediate activation distributions. To mitigate this issue, the optimization could be split into several intermediate subproblems with endpoint positions interpolated between the initial and final desired locations, such that the obstacle avoidance constraint is imposed in each intermediate optimization problem. In general, the resolution of this intermediate problem discretization, that continuously achieves no obstacle intersection, is a function of the objective, the arm's architecture, and the obstacle geometry.

While the centerlines of the optimized configurations in cases (a)-(c) are qualitatively similar, the geometrical distribution of the activated fiber regions varies greatly between the three deformed filaments. Further, the optimized activation parameters $\boldsymbol{\Gamma}^{\mathcal{G}}$ differ significantly among the three fiber fields, despite the piecewise activation forms $\gamma^{(i)}(\theta)$ being defined by the same parameters $N^{(i)}$, $\theta_0^{(i)}$, and $\sigma^{(i)}$ $(i = 1, 2)$ in each fiber field. The activation distribution in fiber field (a) is dominated by the activity in the helical fiber ring, while the activation magnitudes in (b) are larger in the uniaxial fiber ring. The activation is roughly evenly distributed across the two rings in the case of the fiber field (c).

Interestingly, the fiber field in (d) generated the only optimal activation where the filament wraps clockwise around the obstacle. Under the prescribed constraints, the filament in (d) does not reach the target endpoint by wrapping counterclockwise, since the larger right-handed helical angle of $\pi/5$ yields too large of a torsion when curling counterclockwise upon fibrillar contraction. As a result, the manipulator in (d) cannot reach the target endpoint, given that the clockwise path around the obstacle requires a longer centerline.

From an actuation standpoint, the target configuration objective (ii) is much more challenging to achieve exactly with $J^{\mathcal{G}} = 0$, since an exact match would require all points $\mathcal{Z}$ of the manipulator's centerline to overlap with the points $\mathcal{S}$ on the target curve. As such, it is generally considered satisfactory to achieve an arbitrary target configuration in an approximate sense. In fiber fields (a) and (b), the optimized activation results in a very close match between the deformed filament and the target curve. However, in the case of fiber fields (c) and (d), the optimization procedure did not locate a satisfactory minimum of $J^{\mathcal{G}}$ under the imposed constraints.

The quality of the target configuration match for fiber field (c) is worse likely because it does not contain rings that permit distinct modes of actuation. In particular, for both (a) and (b), the first ring with uniaxial fibers is responsible for generating curvature, while the second ring with helical fibers generates curvature as well as twist and torsion, as previously demonstrated in Fig. 2. In contrast, both rings in fiber field (c) contain only helical fibers, reducing the amount of direct control over the curvature of the filament. Nonetheless, it

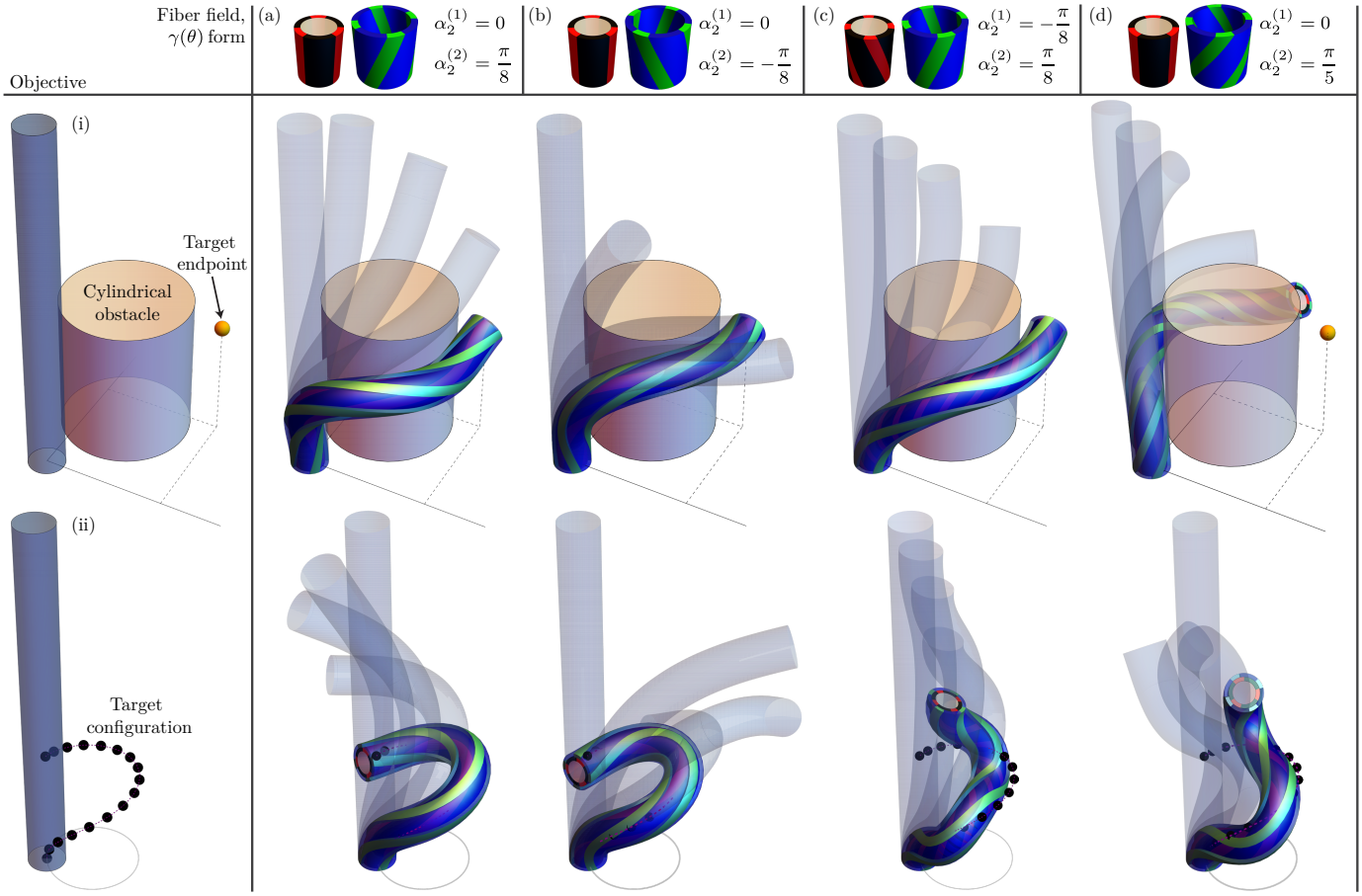


Fig. 3. Results of optimizing fiber activation in soft arms with multi-ring fiber fields under more involved optimization objectives. Three two-ring fiber fields are considered: (a) uniaxial and right-handed helical ($\alpha_2^{(2)} = \pi/8$), (b) uniaxial and left-handed helical ($\alpha_2^{(2)} = -\pi/8$), (c) left-handed helical ($\alpha_2^{(1)} = -\pi/8$) and right-handed helical ($\alpha_2^{(2)} = \pi/8$), (d) uniaxial and right-handed helical ($\alpha_2^{(2)} = \pi/5$). The filaments with each of the four fiber fields are optimized under two optimization objectives: (i) a target endpoint position objective with $\boldsymbol{r}^{\mathcal{G}}_{\text{end}} = \frac{1}{3}(L, L, L)$ with the constraint $\mathcal{C} = \{\boldsymbol{r}(Z) \notin \mathcal{D}\}$, where $\mathcal{D}$ represents a cylindrical obstacle, (ii) a target configuration defined by a target curve $\boldsymbol{r}^{\mathcal{G}}(t)$, which the centerline $\boldsymbol{r}$ is meant to match. Fiber fields in (a) and (b) successfully fulfill objective (i), and their centerlines approximately match the target configuration in objective (ii). However, the filament in (c) does not achieve objective (ii), and the filament in (d) fails to fulfill both objectives. The radius of the cylindrical obstacle region $\mathcal{D}$ is augmented by a scalar corresponding to the outer radius of the filament, so that the filament body does not intersect the obstacle. The target curve in objective (ii) is given by $\boldsymbol{r}^{\mathcal{G}}(t) = \mathbf{R}\tilde{\boldsymbol{r}}^{\mathcal{G}}(t)$, where $\tilde{\boldsymbol{r}}^{\mathcal{G}}(t) = (-1.2 + 1.2\cos(2t), 2.4\cos(t)\sin(t), 2.8 + 0.35(-2+t)^3)$, and $\mathbf{R}$ is a clockwise rotation transformation by an angle $5\pi/6$. The sets $\mathcal{Z}$ and $\mathcal{S}$ use 17 uniformly-spaced points in the intervals $Z \in [0, L]$, and $t \in [0, 3]$, respectively.

should be noted that fiber field (c) provides more versatile actuation than a single-ring helical fiber field. That is, the interaction of two rings with helical fibers of opposite handedness, such as cancellation of components contributing to torsion generation, can result in configurations otherwise unachievable by a single-ring filament.

Notably, the robotic arm in (d) also does not achieve a satisfactory match with the target configuration, even though it contains both uniaxial and helical fiber rings. In this case, the decreased matching quality occurs because the multi-ring field in (d) contains densely packed helical fibers due to the higher helical angle of $\pi/5$. The dense fiber helix generates larger twist for the same activation magnitudes compared to lower helical angle values, making it less effective at matching low-torsion configurations, e.g., the chosen $\boldsymbol{r}^{\mathcal{G}}(t)$.

V. Conclusion

In this letter, we propose a physics-informed methodology for the control of fiber-reinforced soft robotic arms. By using the reduced-order active filament model, we can predict the shape of a fiber-reinforced arm in real time. Importantly, the model that we used to describe the soft arm mechanics follows rigorous continuum mechanics developments, such that any compromises in model fidelity stem only from the employed dimensional reduction. Motivated by the real-time computational capabilities of the model, we applied the active filament theory to tackle the quasi-static control of fiber-reinforced filamentary robotic arms. In particular, we stated the control problem as a minimization of the deviation of the current arm shape properties from the desired target properties of the arm's shape. Our optimization approach considers the space of all admissible fibrillar activations to compute one possible solution to the inverse problem of control objective matching. To evaluate the performance of the proposed methodology, we presented the results of several computational experiments for both single-ring and multi-ring fiber fields. We found that the low computational cost of the utilized model permitted almost instantaneous computation of the optimal fibrillar activation.

TABLE I
MINIMIZING ACTIVATION PARAMETERS AND CENTERLINE CONTRACTION FOR ALL EVALUATED FIBER FIELDS AND OBJECTIVES.

Scenario	Activation parameters	$L_{\boldsymbol{\Gamma}}/L$
Fig. 2(a)	$\bar{\gamma}^{\mathcal{G}} \approx -(2.170, 2.048, 1.716)$	0.6755
Fig. 2(b)	$\bar{\gamma}^{\mathcal{G}} \approx -(1.486, 0.223, 1.108)$	0.8732
Fig. 2(c)	$\bar{\gamma}^{\mathcal{G}} \approx -(0.094, 1.965, 0.000)$	0.9073
Fig. 2(d)	$\bar{\gamma}^{\mathcal{G}} \approx -(3.521, 0.000, 1.066)$	0.8584
Fig. 3(a)(i)	$\bar{\gamma}^{\mathcal{G}(1)} \approx -(0.000, 1.696, 0.099)$ $\bar{\gamma}^{\mathcal{G}(2)} \approx -(0.016, 0.000, 3.219, 2.865)$	0.8940
Fig. 3(b)(i)	$\bar{\gamma}^{\mathcal{G}(1)} \approx -(3.250, 0.001, 2.925)$ $\bar{\gamma}^{\mathcal{G}(2)} \approx -(1.964, 1.715, 2.705, 0.754)$	0.8046
Fig. 3(c)(i)	$\bar{\gamma}^{\mathcal{G}(1)} \approx -(0.003, 6.096, 0.001, 4.204)$ $\bar{\gamma}^{\mathcal{G}(2)} \approx -(3.380, 3.975, 2.028, 6.565)$	0.7060
Fig. 3(d)(i)	$\bar{\gamma}^{\mathcal{G}(1)} \approx -(0.000, 4.395, 2.004)$ $\bar{\gamma}^{\mathcal{G}(2)} \approx -(1.722, 1.191, 0.552, 0.962)$	0.8516
Fig. 3(a)(ii)	$\bar{\gamma}^{\mathcal{G}(1)} \approx -(1.541, 0.000, 2.896)$ $\bar{\gamma}^{\mathcal{G}(2)} \approx -(3.913, 0.000, 0.000, 4.729)$	0.8167
Fig. 3(b)(ii)	$\bar{\gamma}^{\mathcal{G}(1)} \approx -(5.727, 0.000, 0.000)$ $\bar{\gamma}^{\mathcal{G}(2)} \approx -(1.408, 0.000, 3.026, 2.403)$	0.8162
Fig. 3(c)(ii)	$\bar{\gamma}^{\mathcal{G}(1)} \approx -(8.000, 0.000, 0.000, 4.298)$ $\bar{\gamma}^{\mathcal{G}(2)} \approx -(4.422, 0.680, 0.970, 6.014)$	0.7341
Fig. 3(d)(ii)	$\bar{\gamma}^{\mathcal{G}(1)} \approx -(4.623, 0.000, 1.931)$ $\bar{\gamma}^{\mathcal{G}(2)} \approx -(5.293, 0.000, 0.000, 7.163)$	0.7828

The computational experiments demonstrated that arms with single-ring helical fiber fields might not be able to access a range of positions with their end effectors if feasibility constraints are imposed on the fiber activation magnitudes. On the other hand, introducing an additional ring with a different fiber field architecture to the soft arm could greatly enrich the space of reachable configurations, and enable more advanced control, e.g., involving reliable obstacle avoidance.

We performed the evaluation of the control methodology in a computational environment, so the proposed approach would benefit from experimental validation using matching soft-robotic prototypes. Further, eqs. (3)-(6) do not provide the internal stresses in the manipulator developed due to fibrillar activation, but they do inform the energy required for the deformation. Using the system's energy, all stresses could be extracted by integrating the Kirchhoff equations [16], including the forces that the manipulator exerts on its surroundings. For a given actuation model, the energy would also describe the force-generation requirements of the fibers in an engineering implementation. Finally, our method relies on the assumption of quasi-static deformation in response to fibrillar activation. Thus, future work could incorporate actuation dynamics into the utilized active filament model to enable the use of state-of-the-art feedback control solutions.

REFERENCES

[1] D. Trivedi, C. D. Rahn, W. M. Kier, and I. D. Walker, "Soft Robotics: Biological Inspiration, State of the Art, and Future Research," *Applied Bionics and Biomechanics*, vol. 5, no. 3, pp. 99–117, 2008.

[2] R. Ortega and M. W. Spong, "Adaptive motion control of rigid robots: A tutorial," *Automatica*, vol. 25, no. 6, pp. 877–888, Nov. 1989.

[3] C. Abdallah, D. Dawson, P. Dorato, and M. Jamshidi, "Survey of robust control for rigid robots," *IEEE Control Systems Magazine*, vol. 11, no. 2, pp. 24–30, Feb. 1991.

[4] L. Sciavicco and B. Siciliano, *Modelling and Control of Robot Manipulators*. Springer Science & Business Media, Feb. 2001.

[5] D. Zhang and B. Wei, "A review on model reference adaptive control of robotic manipulators," *Annual Reviews in Control*, vol. 43, pp. 188–198, Jan. 2017.

[6] T. George Thuruthel, Y. Ansari, E. Falotico, and C. Laschi, "Control Strategies for Soft Robotic Manipulators: A Survey," *Soft Robotics*, vol. 5, no. 2, pp. 149–163, Apr. 2018.

[7] T. G. Thuruthel, E. Falotico, F. Renda, and C. Laschi, "Model-Based Reinforcement Learning for Closed-Loop Dynamic Control of Soft Robotic Manipulators," *IEEE Transactions on Robotics*, vol. 35, no. 1, pp. 124–134, Feb. 2019.

[8] D. Rus and M. T. Tolley, "Design, fabrication and control of soft robots," *Nature*, vol. 521, no. 7553, pp. 467–475, May 2015.

[9] C. Della Santina, R. K. Katzschmann, A. Biechi, and D. Rus, "Dynamic control of soft robots interacting with the environment," in *2018 IEEE International Conference on Soft Robotics (RoboSoft)*, Apr. 2018, pp. 46–53.

[10] A. W. Feinberg, "Biological Soft Robotics," *Annual Review of Biomedical Engineering*, vol. 17, no. 1, pp. 243–265, 2015.

[11] K. Nakajima, H. Hauser, R. Kang, E. Guglielmino, D. Caldwell, and R. Pfeifer, "A soft body as a reservoir: Case studies in a dynamic model of octopus-inspired soft robotic arm," *Frontiers in Computational Neuroscience*, vol. 7, 2013.

[12] Z. Xie, A. G. Domel, N. An, C. Green, Z. Gong, T. Wang, E. M. Knubben, J. C. Weaver, K. Bertoldi, and L. Wen, "Octopus Arm-Inspired Tapered Soft Actuators with Suckers for Improved Grasping," *Soft Robotics*, vol. 7, no. 5, pp. 639–648, Oct. 2020.

[13] Q. Guan, J. Sun, Y. Liu, N. M. Wereley, and J. Leng, "Novel Bending and Helical Extensile/Contractile Pneumatic Artificial Muscles Inspired by Elephant Trunk," *Soft Robotics*, vol. 7, no. 5, pp. 597–614, Oct. 2020.

[14] Y. Zhang, D. Yang, P. Yan, P. Zhou, J. Zou, and G. Gu, "Inchworm Inspired Multimodal Soft Robots With Crawling, Climbing, and Transitioning Locomotion," *IEEE Transactions on Robotics*, pp. 1–14, 2021.

[15] B. Kaczmarski, D. E. Moulton, E. Kuhl, and A. Goriely, "Active filaments I: Curvature and torsion generation," *Journal of the Mechanics and Physics of Solids*, vol. 164, p. 104918, July 2022.

[16] D. E. Moulton, T. Lessinnes, and A. Goriely, "Morphoelastic rods III: Differential growth and curvature generation in elastic filaments," *Journal of the Mechanics and Physics of Solids*, vol. 142, p. 104022, Sept. 2020.

[17] N. Naughton, J. Sun, A. Tekinalp, T. Parthasarathy, G. Chowdhary, and M. Gazzola, "Elastica: A Compliant Mechanics Environment for Soft Robotic Control," *IEEE Robotics and Automation Letters*, vol. 6, no. 2, pp. 3389–3396, Apr. 2021.

[18] F. Renda, C. Messer, C. Rucker, and F. Boyer, "A Sliding-Rod Variable-Strain Model for Concentric Tube Robots," *IEEE Robotics and Automation Letters*, vol. 6, no. 2, pp. 3451–3458, Apr. 2021.

[19] N. K. Uppalapati and G. Krishnan, "VaLeNS: Design of a Novel Variable Length Nested Soft Arm," *IEEE Robotics and Automation Letters*, vol. 5, no. 2, pp. 1135–1142, Apr. 2020.

[20] G. Kirchhoff, "Ueber das Gleichgewicht und die Bewegung eines unendlich dünnen elastischen Stabes." vol. 1859, no. 56, pp. 285–313, Jan. 1859.

[21] D. E. Moulton, T. Lessinnes, and A. Goriely, "Morphoelastic rods. Part I: A single growing elastic rod," *Journal of the Mechanics and Physics of Solids*, vol. 61, no. 2, pp. 398–427, Feb. 2013.

[22] F. Connolly, C. J. Walsh, and K. Bertoldi, "Automatic design of fiber-reinforced soft actuators for trajectory matching," *Proceedings of the National Academy of Sciences*, vol. 114, no. 1, pp. 51–56, Jan. 2017.

[23] I. Gravagne, C. Rahn, and I. Walker, "Large deflection dynamics and control for planar continuum robots," *IEEE/ASME Transactions on Mechatronics*, vol. 8, no. 2, pp. 299–307, June 2003.